Research Article | Vol. 27, No. 18 / 2 September 2019 / Optics Express 25749
Optics EXPRESS

An extended quantitative model for super-resolution optical fluctuation imaging (SOFI)

WIM VANDENBERG,[1,2,4] MARCEL LEUTENEGGER,[3] SAM DUWÉ,[1] AND PETER DEDECKER[1,5]

[1]Department of Chemistry, KU Leuven, Celestijnenlaan 200G, 3000 Leuven, Belgium
[2]Univ. Lille, CNRS, UMR 8516 - LASIR, F-59000 Lille, France
[3]Max Planck Institute for Biophysical Chemistry, Department of NanoBiophotonics, Am Faßberg 11, 37077 Göttingen, Germany
[4]wim.vandenberg@kuleuven.be
[5]peter.dedecker@kuleuven.be

Abstract: Super-resolution optical fluctuation imaging (SOFI) provides super-resolution (SR) fluorescence imaging by analyzing fluctuations in the fluorophore emission. The technique has been used both to acquire quantitative SR images and to provide SR biosensing by monitoring changes in fluorophore blinking dynamics. Proper analysis of such data relies on a fully quantitative model of the imaging. However, previous SOFI imaging models made several assumptions that can not be realized in practice. In this work we address these limitations by developing and verifying a fully quantitative model that better approximates real-world imaging conditions. Our model shows that (i) SOFI images are free of bias, or can be made so, if the signal is stationary and fluorophores blink independently, (ii) allows a fully quantitative description of the link between SOFI imaging and probe dynamics, and (iii) paves the way for more advanced SOFI image reconstruction by offering a computationally fast way to calculate SOFI images for arbitrary probe, sample and instrumental properties.

1. Introduction

Super-resolution optical fluctuation imaging (SOFI) provides a sub-diffraction spatial resolution in far-field fluorescence microscopy by making use of spontaneous fluctuations in the fluorophore emission [1]. SOFI distinguishes itself from other diffraction-unlimited techniques in its ability to operate across a wide range of experimental conditions such as low probe brightness or high background emission [2–5] and its use of conventional equipment. In addition, the necessary software to perform the imaging is readily available [6]. The technique also lends itself well to validation by a framework for quantifying the signal to noise level [7] and the availability of dual-mode probes [8]. This has led to the application of the technique in 'difficult' conditions either imposed by the sample [9–11] or deriving from the combination with advanced acquisition schemes [12–14].

The resulting SOFI images have been used to perform quantitative imaging, such as determining the distribution of membrane microdomains [15], or the distributions of biological interactions at the SR level [9]. Recently, the technique was also used in a novel way to obtain contrast at the SR level by visualizing changes in the fluorophore dynamics in space and time [10]. In this work, SOFI was combined with a genetically-encoded biosensor for kinase activity, in which activation of the kinase caused a conformational change of the biosensor and concomitant change in its fluorescence blinking. Using changes in blinking as a contrast mechanism has been previously applied, e.g. in TRAST microscopy [16], though SOFI is one of the only techniques that can provide this information at the SR level.

#359686 https://doi.org/10.1364/OE.27.025749
Journal © 2019 Received 6 Feb 2019; revised 12 Apr 2019; accepted 20 May 2019; published 27 Aug 2019

Optics EXPRESS

Crucial for this analysis is the availability of a model that quantitatively describes the link between the fluorophore distribution and properties, and the resulting SOFI image. A candidate model was developed already in the original SOFI publication [1], and was subsequently refined [17,18]. Most notably, this model shows that SOFI imaging is bias-free, in the sense that the image will be a correct representation of the fluorophore distribution in the sample, provided that the underlying assumptions of SOFI are satisfied: the sample is labelled with fluorophores that display mutually independent fluorescence dynamics, and the fluorescence emission is stationary. Strict stationarity is difficult to realize, but we have found that in biological imaging the fluorescence emission is usually sufficiently stationary despite some probe movement or photo-bleaching of fluorophores [19,20]. This simple model was further extended to capture changes in blinking dynamics in a way that is independent of the probe concentration [10].

While this analytical model has proven highly useful, it does require assumptions that cannot be met in practice. In particular, it assumes an infinite measurement duration, and a detector capable of instantaneously measuring the fluorescence intensity at any position and any time in the sample. Unfortunately, none of us are able to do infinite measurements, while actual detectors use discrete sampling in which the fluorescence is integrated over each pixel in space and in time. Despite its importance, this model can therefore only be considered as an approximation to actual measurement conditions, where the quality of this approximation is difficult to assess. This complicates the quantitative analysis of SOFI images, especially when the model would be applied to extraction of molecular parameters [18,21].

In this work we advance a full theoretical model of SOFI imaging, which takes into account the finite measurement duration and the characteristics of real-world detectors, and that is sufficiently general to accommodate future developments in hardware and probes. Our work (i) shows that SOFI images are indeed free of bias, or can be made so, if the signal is stationary and fluorophores blink independently, (ii) allows a fully quantitative description of the link between SOFI imaging and probe dynamics under real-world imaging conditions, and (iii) paves the way for more advanced SOFI image reconstruction by offering a computationally fast way to calculate SOFI images for arbitrary probe, sample and instrumental properties.

2. Brief review of SOFI theory

We start by summarizing the theory of SOFI imaging for a perfect and infinitely-sampled detector [1,17,18,22]. A more detailed overview can be found in [7].

In SOFI, a camera consisting of an two-dimensional array of pixels records multiple fluorescence images from the same sample, labeled with fluorophores that display spontaneous dynamics in their fluorescence emission. The resulting fluorescence images make up a dataset $F(\mathbf{r}, t)$, denoting the fluorescence at time t observed by the detector pixel looking at the sample position $\mathbf{r}$. In the absence of noise (excluding shot noise as well), the emission from M fluorophores located at positions $\{\mathbf{r}_j\}$ is given by

$$F(\mathbf{r}, t) = \sum_{j=1}^{M} \mathrm{PSF}(\mathbf{r} - \mathbf{r}_j)\epsilon_j s_j(t) \tag{1}$$

where $\mathrm{PSF}(\mathbf{r})$ is the point spread function (PSF) of the instrument, ϵ_j is the brightness of the j^{th} molecule (expressed in units of detector output per unit of time), and $s_j(t)$ is an indicator function that describes whether the molecule is in an emissive state at time t ($0 \leq s_j(t) \leq 1$).

$F(\mathbf{r}, t)$ is not constant in time due to the fluctuations of the fluorophores, which means that the fluorescence seen at any position $\mathbf{r}$ consists of samples from a distribution specific to that position. SOFI analyzes these distributions by calculating their cumulants, where the values of these cumulants become the pixel values in the SOFI image.

Optics EXPRESS

An infinite number of cumulants can be defined and classified according to their order $k \in \mathbb{N}$. In practice, second- to fifth-order cumulants are the most relevant for SOFI. A SOFI calculation of order k corresponds to the convolution of a distribution proportional to the local fluorophore concentration with the PSF raised to the power k. This leads to a $\sqrt{k}$-fold improvement in spatial resolution, or up to k-fold if deconvolution is performed [17]. To provide adequate sampling of the enhanced resolution, cumulant images can be resampled on a k-fold finer virtual pixel grid by calculating cross-cumulants among different detector pixels [17]. Alternatively, Fourier interpolation can be used [22]. Cross-cumulants among mutually delayed fluorescence traces can be calculated as well, where the extent of this delay is known as the 'time lag', and can be used to analyze the blinking characteristics of the fluorophores [23]. As an example, for a second-order SOFI image $\kappa_2(\mathbf{r})$ using a cross-cumulant between pixels separated by ξ and time lag δ, we calculate

$$\begin{aligned}\kappa_2\left(\mathbf{r}+\frac{\boldsymbol{\xi}}{2}\right) &= C_2\left(F(\mathbf{r},t), F(\mathbf{r}+\boldsymbol{\xi}, t+\delta)\right) \\ &= \mathrm{PSF}\left(\frac{\boldsymbol{\xi}}{\sqrt{2}}\right)\sum_j^M \mathrm{PSF}^2\left(\mathbf{r}+\frac{\boldsymbol{\xi}}{2}-\mathbf{r}_j\right)\epsilon_j^2 C_2(\delta),\end{aligned} \tag{2}$$

where we assumed a Gaussian PSF. $C_2(\delta)$ is a function determined by the characteristics of the fluorophores and the instrument. In general the nature of this function is not investigated further, but it is rather assumed that it is identical for all fluorophores in the sample. Only if this assumption holds is the cumulant $\kappa_k(\mathbf{r})$ proportional to the local fluorophore concentration. Clearly, this assumption is required for linearity in classical fluorescence imaging as well because the average intensity is $\kappa_1(\mathbf{r}) = C_1\left(F(\mathbf{r},t)\right)$. However, the dependence of the SOFI imaging on $C_2(\delta)$ is also the reason that this technique can be used for the SR visualization of blinking heterogeneity.

While this analysis provides detailed and quantitative insight into the SOFI imaging process, it does not fully account for the conditions encountered in experiments, where the measurement duration is finite, $F(\mathbf{r},t)$ is integrated by the detector pixels both in space and time, and the PSF is non-Gaussian. In the following, we expand the SOFI model to include these effects, aiming to substantially improve the quantitative interpretation of SOFI images.

3. The general theoretical foundation of SOFI

3.1. An applied review of distribution theory

SOFI imaging consists of calculating cumulants of the fluorescence distributions observed at every position of the sample. Here, we aim to develop a model for these cumulants given the properties of the fluorophores and the instrument. Fortunately, we need only consider the signal of a single fluorophore, since cumulants are additive as long as the fluorescence dynamics of the molecules are independent [24]:

$$C_k\left(\sum_j F_j\right) = \sum_j C_k\left(F_j\right) \tag{3}$$

To derive the cumulant C_k, we start from the cumulant generating function (CGF) as defined in [24]:

$$\mathrm{CGF}(t_1, t_2, \ldots) = \log\left(\mathrm{CF}(t_1, t_2, \ldots)\right), \tag{4}$$

where

$$\mathrm{CF}(t_1, t_2, \ldots) = \mathbb{E}\left\{\exp\left(\mathrm{i}t_1X_1 + \mathrm{i}t_2X_2 + \cdots\right)\right\} \tag{5}$$

stands for the characteristic function and X_j represents the signal measured by camera pixel j. $\mathbb{E}\{\ldots\}$ denotes the expectation value over all X_j and i is the imaginary unit. In second order

Optics EXPRESS

SOFI, for example, X_1 and X_2 represent the signals detected by the two pixels that are being considered, related to variables t_1 and t_2 in the associated CGF. It is straightforward to calculate the $(k = m + n + \cdots)^{\text{th}}$-order cumulant given knowledge of the CGF [24]:

$$C_k(X_1^m, X_2^n, \ldots) = \mathrm{i}^{-k} \left[\frac{\partial^m}{\partial t_1^m} \frac{\partial^n}{\partial t_2^n} \cdots \mathrm{CGF}(t_1, t_2, \ldots) \right]_{t_1, t_2, \ldots = 0} \tag{6}$$

These equations, combined with the additivity of cumulants, reduce the problem of knowing the cumulants for an arbitrary sample to knowing the CGF of a single molecule. In what follows, we will tackle this question in two steps: first we will derive the CGF for a non-blinking fluorophore imaged using two types of detectors, which we will then expand to take blinking into account. Finally, we will develop easier-to-use specializations of our model for specific types of imaging and fluorescence dynamics.

3.2. Cumulant generating functions of detectors

3.2.1. Low read-out noise sensors

With an ideal camera, the only source of measurement noise is the shot noise intrinsic to the emission/detection process. In that case the CGF for a single pixel is that of the Poisson distribution [24]:

$$\mathrm{CGF}_{\mathrm{poisson}}(t) = \lambda \left(\mathrm{e}^{\mathrm{i}t} - 1 \right), \tag{7}$$

where λ is the expected number of photons detected by the pixel, given by the product of the detection probability and the expected amount of photons the dye emits during the exposure time. Since the shot noise is independent among different pixels, Eqs. (4) and (5) show that the compound detection CGF is given by

$$\mathrm{CGF}_{\mathrm{nn}}(t_1, t_2, \ldots) = \sum_j \lambda_j \left(\mathrm{e}^{\mathrm{i}t_j} - 1 \right) \tag{8}$$

where λ_j is the expected number of detected photons associated with each pixel j. This CGF serves as an idealized model for sCMOS or CCD cameras that feature low read-out noise (nn: negligible noise).

3.2.2. Electron-multiplying sensors

An electron-multiplying CCD camera (EM-CCD) contributes excess noise due to the amplification process. This electron multiplication process can be modelled as a gamma distribution [25], whose CF is

$$\mathrm{CF}_{\mathrm{gamma}} = (1 - \gamma \mathrm{i}t)^{-\eta}, \tag{9}$$

where η is the number of generated photo-electrons before the amplification register and γ is the amplification gain. We can now compound this distribution with the Poisson noise intrinsic to the stochastic nature of photon detection using Eq. (5). The Taylor series expansion of the exponential function allows us to simplify the CF:

$$\begin{aligned} \mathrm{CF}_{\mathrm{em}} &= \sum_{\eta=0}^{\infty} (1 - \gamma \mathrm{i}t)^{-\eta} \frac{\lambda^\eta \mathrm{e}^{-\lambda}}{\eta!} \\ &= \mathrm{e}^{-\lambda} \sum_{\eta=0}^{\infty} \frac{(\lambda/(1 - \gamma \mathrm{i}t))^\eta}{\eta!} \\ &= \exp\left(\frac{\lambda \gamma \mathrm{i}t}{1 - \gamma \mathrm{i}t} \right) \end{aligned} \tag{10}$$

Optics EXPRESS

As before, this result easily extends to multiple pixels by using the independence of the noise among the pixels,

$$\mathrm{CGF}_{\mathrm{em}}(t_1, t_2, \ldots) = \sum_j \frac{\lambda_j \gamma \mathrm{i} t_j}{1 - \gamma \mathrm{i} t_j}, \tag{11}$$

with variables λ_j and t_j for the contributing pixels of the detector.

3.2.3. Consistency check

We can check the detection CGFs (8) and (11) by calculating the expected signal-to-noise ratio (SNR), that is the ratio of mean signal over the standard deviation:

$$\mathrm{SNR} = \left. \frac{\frac{\partial}{gt}\mathrm{CGF}}{\sqrt{\frac{\partial^2}{\partial t^2}\mathrm{CGF}}} \right|_{t=0} \tag{12}$$

For the ideal camera $\mathrm{CGF}_{\mathrm{nn}}$ we obtain $\mathrm{SNR} = \sqrt{\lambda}$ as expected for pure shot noise, whereas our $\mathrm{CGF}_{\mathrm{em}}$ for electron-multiplying cameras yields $\mathrm{SNR} = \sqrt{\lambda/2}$ in line with the characteristic, well-known excess noise factor.

It should be noted that both the low noise and the electron multiplying detector have a CGF of the form:

$$\mathrm{CGF}_{\text{linear detector}} = \sum_j \lambda_j f(t_j) \tag{13}$$

In practical terms, this expresses that the signal in each pixel is read out independently, and that the camera does not display non-linearities in its response to light of varying intensities. The following discussions and conclusions apply to any detector that meets these conditions.

3.3. Effect of blinking on the cumulant generating function

We now add blinking of the fluorophores to our model. We start with a general description that is valid for any type of fluorescence dynamics, before introducing descriptions of specific blinking models in section 5.

Within the context of a temporally-integrating detector, blinking of the fluorophores can be incorporated by scaling the brightness of the fluorophore by the fraction ρ, which is the fraction of time the fluorophore spent in emissive states during the exposure time T. This on-time ratio ρ is obtained as

$$\rho(t) = \frac{1}{T} \int_t^{t+T} s\,(t)\,\mathrm{d}t, \tag{14}$$

where we use the indicator function of Eq. (1). Because the blinking is stochastic, the on-time ratio observed for a molecule *in a particular acquired fluorescence image* can strongly differ between fluorescence images. We model this as variations in ρ subject to its probability distribution, $\phi(\rho)$, determined by the dynamics of the blinking.

We take blinking into account by compounding the detector model $\mathrm{CGF}_{\mathrm{det}}$ with $\phi(\rho)$, using the fact that $\mathrm{CGF}_{\mathrm{det}}$ follows the conditions of Eq. (13):

$$\mathrm{CGF}^*_{\mathrm{det}}(t_1, t_2, \ldots) = \log\left(\int_0^1 \exp\left(\rho\, \mathrm{CGF}_{\mathrm{det}}(t_1, t_2, \ldots)\right) \phi(\rho)\, \mathrm{d}\rho \right), \tag{15}$$

where the observed brightness of a blinking fluorophore is $\rho\lambda$, with λ the brightness that would be observed if the fluorophore were continuously emitting. If we denote the cumulant generating

Optics EXPRESS

function of $\phi(\rho)$ as CGF_ρ, then we obtain the CGF^* of blinking fluorophores:

$$\mathrm{CGF}^*_{\mathrm{det}}(t_1, t_2, \ldots) = \mathrm{CGF}_\rho \left(\mathrm{i}^{-1}\, \mathrm{CGF}_{\mathrm{det}}(t_1, t_2, \ldots) \right) \tag{16}$$

That is we obtain the CGF^* by evaluating the on-time ratio CGF_ρ for an argument value given by the detection $\mathrm{CGF}_{\mathrm{det}}$.

Inserting now the detection $\mathrm{CGF}_{\mathrm{nn}}$ for low-noise sensors yields

$$\mathrm{CGF}^*_{\mathrm{nn}}(t_1, t_2, \ldots) = \mathrm{CGF}_\rho \left(\frac{1}{\mathrm{i}} \sum_j \lambda_j \left(\mathrm{e}^{\mathrm{i}t_j} - 1 \right) \right). \tag{17}$$

Similarly for an electron-multiplying camera we get

$$\mathrm{CGF}^*_{\mathrm{em}}(t_1, t_2, \ldots) = \mathrm{CGF}_\rho \left(\sum_j \frac{\lambda_j \gamma t_j}{1 - \gamma \mathrm{i} t_j} \right). \tag{18}$$

Using Eq. (6) and the chain rule of differentiation, we can now calculate all possible cumulants for a blinking fluorophore. Assuming that all pixels are distinct, for an ideal camera we obtain:

$$C_2(X_1, X_2) = \lambda_1 \lambda_2\, C_2(\rho) \tag{19}$$

$$C_3(X_1, X_2, X_3) = \lambda_1 \lambda_2 \lambda_3\, C_3(\rho) \tag{20}$$

$$\begin{aligned} C_4(X_1, X_2, X_3, X_4) &= \lambda_1 \lambda_2 \lambda_3 \lambda_4\, C_4(\rho) \\ &\ldots \end{aligned} \tag{21}$$

where X_j is the j-th pixel on the detector, and $C_k(\rho)$ is the k^{th}-order cumulant of the on-time ratio distribution.

To take into account time lags, we need to consider the joint probability distribution of ρ at the distinct time lags. In the following, X_{j,δ_i} denotes the intensity trace measured by pixel j with a time lag of δ_i. Accordingly, we expand $\phi(\rho)$ into the matching probability distribution function of a multivariate distribution $\phi(\rho, \rho_{\delta_1}, \rho_{\delta_2}, \ldots)$. This results in the following cumulants for a detector with negligible noise:

$$C_2(X_1, X_{1,\delta_1}) = \lambda_1^2\, C_2(\rho, \rho_{\delta_1}) \tag{22}$$

$$C_2(X_1, X_{2,\delta_1}) = \lambda_1 \lambda_2\, C_2(\rho, \rho_{\delta_1}) \tag{23}$$

$$C_3(X_1, X_{1,\delta_1}, X_{1,\delta_2}) = \lambda_1^3\, C_3(\rho, \rho_{\delta_1}, \rho_{\delta_2}) \tag{24}$$

$$C_3(X_1, X_2, X_{3,\delta_1}) = \lambda_1 \lambda_2 \lambda_3\, C_3(\rho, \rho, \rho_{\delta_1}) \tag{25}$$

$$C_3(X_1, X_{1,\delta_1}, X_2) = \lambda_1^2 \lambda_2\, C_3(\rho, \rho, \rho_{\delta_1}) \tag{26}$$

and analogous expressions for higher orders. These equations are the fundamental equations that describe SOFI imaging. In the following sections we will provide expressions for λ and the cumulants of ρ.

For an electron-multiplying camera, Eqs. (19)–(26) are multiplied by the gain γ raised to the power k of the cumulant order:

$$C_{k,\mathrm{em}} = \gamma^k C_{k,\mathrm{nn}} \tag{27}$$

It turns out (Appendix A) that these calculations become much more complex if intensity traces in the cross-cumulants are used repeatedly from the same pixel and equal lag time. However, image reconstructions in SOFI should rely on cross-cumulants of intensity traces from strictly different pixels and/or lag times anyway: auto-cumulants are biased by noise, thus to be avoided; and cross-cumulants with repeated use of intensity traces yield reduced SNR because the noise in reused intensity traces is raised to a higher power.

Optics EXPRESS

3.4. Effect of finite measurement durations

Any experimentally estimated cumulant value will only asymptotically approach the true value for an infinite number of fluorescence images. In practice, one is of course limited by photodestruction and phototoxicity. A common correction for photobleaching involves performing the SOFI calculation on a low number of fluorescence images, and then adding or averaging the resulting set of SOFI images [20]. It is therefore natural to ask to what extent these short durations affect the SOFI reconstruction.

The effect of a limited measurement duration can be estimated by replacing the expectation value in the cumulant calculations by experimental averages over a limited number of frames or samples N. In the following, we denote frame-limited cumulants by lower-case c. Application of the formulas in [24] for second-order SOFI leads to:

$$C_2(X_1, X_2) = \mathbb{E}\{X_1 X_2\} - \mathbb{E}\{X_1\}\,\mathbb{E}\{X_2\} \tag{28}$$

$$c_2(X_1, X_2) = \frac{1}{N}\sum_{n=1}^{N}(X_{1,n}X_{2,n}) - \frac{1}{N^2}\sum_{n=1}^{N}X_{1,n}\sum_{n=1}^{N}X_{2,n} \tag{29}$$

$$\begin{aligned}\mathbb{E}\{c_2(X_1, X_2)\} = {} & \frac{N-1}{N}\,\mathbb{E}\left\{X_{1,t}X_{2,t}\right\} \\ & - \sum_{n=1}^{N-1}\frac{N-n}{N^2}\left(\mathbb{E}\left\{X_{1,t+n}X_{2,t}\right\} + \mathbb{E}\left\{X_{1,t}X_{2,t+n}\right\}\right)\end{aligned} \tag{30}$$

We can now simplify Eq. (30) by making use of the symmetry of the derived formulas for time-lags ($\mathbb{E}\left\{X_{1,t}X_{2,t+n}\right\} \equiv \mathbb{E}\left\{X_{1,t+n}X_{2,t}\right\}$ because the *correlated* signal flucations stem from one fluorophore) and substituting with Eq. (28) and variants with time-lag. This leads to Eqs. (31) and (32).

$$\begin{aligned}\mathbb{E}\{c_2(X_1, X_2)\} = {} & \frac{N-1}{N}C_2(X_1, X_2) \\ & - \sum_{n=1}^{N-1} 2\frac{N-n}{N^2}C_2(X_1, X_{2,\delta_n})\end{aligned} \tag{31}$$

$$\begin{aligned}\mathbb{E}\left\{c_2(X_1, X_{2,\delta_s})\right\} = {} & C_2(X_1, X_{2,\delta_s}) - \frac{N-|s|}{N^2}C_2(X_1, X_2) \\ & - \sum_{n=1}^{|s|} 2\frac{N-|s|}{N^2}C_2(X_1, X_{2,\delta_n}) \\ & - \sum_{n=|s|+1}^{N-|s|} 2\frac{N-n}{N^2}C_2(X_1, X_{2,\delta_n}) \\ & - \sum_{n=N-|s|+1}^{N-1} \frac{N-n}{N^2}C_2(X_1, X_{2,\delta_n})\end{aligned} \tag{32}$$

In these equations δ_s is the time-lag applied to the cumulant, that is s exposure times, respectively. We note that the SOFI image calculated for a limited number of fluorescence images N is a linear combination of the SOFI images calculated for all possible time lags. This can complicate the extraction of kinetic information, but does not introduce bias in the imaging since each of these is a valid SOFI image. Further investigation reveals (Appendix B) that the same conclusion holds for third order SOFI imaging, but not for higher orders.

For these higher orders, direct calculation of the cumulant from the experimental data is complicated by the fact that it is no longer an unbiased estimator of the true cumulant. In practical

Optics EXPRESS

terms, this means that the calculated cumulant is distorted by the mixing in of different statistical moments, and sample-dependent deviations can be expected as N gets small. This also implies that the concentration proportionality of the SOFI image is not necessarily maintained across experiments or across different parts of the sample. As for now, this can only be addressed by adapting the estimator of the cumulant so that it is unbiased, conceptually described in Ref. [24]. However, this is outside the scope of this contribution. In practical terms, however, fourth- or higher-order images typically require a high number of fluorescence images, such that this effect is likely to be small in practice, provided that the batch size of the calculation is increased to match.

With these considerations, we have developed a general and extensible model of SOFI imaging. In what follows, we will discuss how this model can be specialized to specific instruments and blinking models.

4. Models for the point spread function

The specifics of the optical instrument determine how the fluorescence photons from a particular molecule are distributed onto the detector, and are therefore highly relevant for our model. As e.g. Eq. (19) shows, the crucial parameter is the number of photo-electrons λ_j that are produced in pixel j in response to a fluorophore located at position $\mathbf{r}_f$. This depends on the brightness of the fluorophore and on how its emitted photons are distributed on the detector by the PSF of the imaging system:

$$\lambda_j = \epsilon_f \iint\limits_{\mathbf{r}\in A_j} \mathrm{PSF}(\mathbf{r}_f - \mathbf{r})\,\mathrm{d}\mathbf{r}, \tag{33}$$

where A_j represents the active detection area of pixel j, and ϵ_f represents the brightness of the fluorophore in its emissive reference state in photons per frame. Care must be taken to correctly take the optical magnification of the system into account.

The previous model of SOFI imaging assumed an ideal point-sampling detector, which is equivalent to taking the limit for $A \to 0$. Equation (33) then reduces to

$$\lambda_j = \epsilon_f\,\mathrm{PSF}(\mathbf{r}_f - \mathbf{r}_j). \tag{34}$$

In practical terms, the strategy is to evaluate Eq. (33) directly for every fluorophore, and to substitute its value into equations such as Eq. (19). For Gaussian PSFs, which cannot be realized in practice yet are widely used as models, the integration in Eq. (33) can be rewritten as

$$\begin{aligned}\lambda_j =& \epsilon_f \left[\Phi\left(\frac{x_j - x_f + d/2}{\sigma}\right) - \Phi\left(\frac{x_j - x_f - d/2}{\sigma}\right)\right] \\ &\times \left[\Phi\left(\frac{y_j - y_f + d/2}{\sigma}\right) - \Phi\left(\frac{y_j - y_f - d/2}{\sigma}\right)\right]\end{aligned} \tag{35}$$

With Φ the cumulative density function of the standard normal distribution, σ the standard deviation of the PSF and d the width of the detector pixel centered at position (x_j, y_j), and for a molecule located at (x_f, y_f).

More realistic PSF models typically do not have clear analytical expressions, but instead emerge from wave-optical calculations or from experimentally measured data. In this case, there usually is no alternative but to evaluate Eq. (33) numerically for each fluorophore and detector pixel, and to substitute these values into the expressions generated by our model, such as Eqs. (19)–(26).

5. Models for the fluorescence dynamics

We now consider the nature of $\phi(\rho)$ for common models of fluorophore blinking. In this paper we will deal exclusively with molecules alternating between two spectroscopic states. This is a

Optics EXPRESS

widespread assumption, and approximates the behavior of organic dyes and fluorescent proteins used as a label for SOFI [26–28]. If different types of blinking are observed [1,29], the results may not be directly applicable and an alternative model for the on-time ratio should be sought. Ultimately, our goal is to derive expressions for $C_k(\rho)$ that can be substituted directly into the equations of our model, such as Eqs. (19)–(26).

5.1. Bernoulli model

The Bernoulli model assumes that molecules do not switch states during the exposure time, but only in between frame exposures. This model is very coarse and serves as a reasonable approximation only for fluorophores whose switching rates $k_{\text{on}\to\text{off}}$ and $k_{\text{off}\to\text{on}}$ are much smaller than the camera frame rate. We consider the Bernoulli model for the simple reason that its CGF is known and trivially extensible to time-lagged cumulants. Details on the derivation are given in [18].

We find that the cumulants depend on $\widehat{\rho}$, the average on-time ratio of the fluorophores. Time-lagged cumulants additionally depend on T/τ, where T represents the exposure time and τ represents the auto-correlation time associated with the blinking. More precisely,

$$1/\tau = k_{\text{on}\to\text{off}} + k_{\text{off}\to\text{on}} \tag{36}$$

$$\widehat{\rho} = \frac{k_{\text{off}\to\text{on}}}{k_{\text{on}\to\text{off}} + k_{\text{off}\to\text{on}}} \tag{37}$$

A number of resulting cumulants are listed in Fig. 1, others can be obtained using the methodology in (Appendix C). As before, the notation $C_2(\rho)$ means a second order cumulant without time lag, while $C_2(\rho, \rho_{\delta_1})$ means a second order cumulant with a time lag of δ_1 images.

Cumulant	Bernoulli cumulant	Correction factor for temporal integration
$C_2(\rho)$	$-\widehat{\rho}^2 + \widehat{\rho}$	$2(T/\tau)^{-2}[T/\tau + \mathrm{e}^{-T/\tau} - 1]$
$C_2(\rho, \rho_{\delta_1})$	$(-\widehat{\rho}^2 + \widehat{\rho})\exp(-\delta_1/\tau)$	$(T/\tau)^{-2}[\mathrm{e}^{-T/\tau}(\mathrm{e}^{T/\tau} - 1)^2]$
$C_3(\rho)$	$2\widehat{\rho}^3 - 3\widehat{\rho}^2 + \widehat{\rho}$	$6(T/\tau)^{-3}[(T/\tau)(1 + \mathrm{e}^{-T/\tau}) + 2(\mathrm{e}^{-T/\tau} - 1)]$

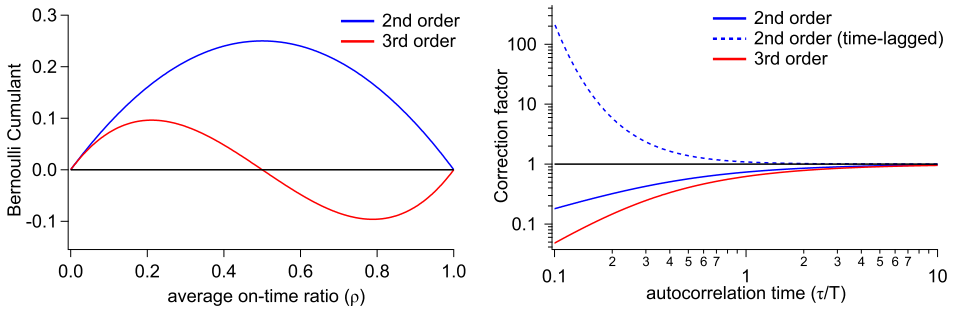

Fig. 1. Cumulants of the Bernoulli distribution and correction factors for fast switching fluorophores. Even though the correction factor for time-lagged second-order SOFI is positive, the absolute signal for a time-lagged cumulant will always be smaller than that of the non-lagged version.

Optics EXPRESS

5.2. Temporally integrated two-state model

In virtually all practical measurements the fluorophores continuously switch between spectroscopic states, independent of the camera acquisition sequence. This means the Bernoulli model cannot explain the experimental behavior of these systems well.

Fortunately, it is possible to derive cumulants for a more complete blinking model (two-state intra-frame switching) by extending the approach of [30] (Appendix C). Up to and including the third-order cumulant this leads to a set of correction factors, function of T/τ, shown in Fig. (1), that need to be multiplied with the corresponding cumulants of the Bernoulli distribution. These correction factors represent the effect of the switching kinetics, whereas the Bernoulli distribution only takes the equilibrium properties into account. These effects can be very pronounced, as shown in Fig. 1.

For higher orders, the cumulant calculations become more complex and can no longer be factored into functions of T/τ and $\widehat{\rho}$. However, the resulting cumulants can still be calculated using the approach described in Appendix C, which will work for all SOFI orders including at most a single non-zero time lag.

Cumulants with more than one time lag can still be calculated using numerical simulations. In practical terms, this means that the blinking of a single fluorophore is simulated for particular values of $k_{\text{on}\to\text{off}}$ and $k_{\text{off}\to\text{on}}$ and T. Doing this over a sufficiently long duration allows the distribution $\phi(\rho)$ to be estimated, and the desired cumulants can be obtained directly.

The absolute kinetics of the blinking are relevant not only in the context of temporal integration of the signal, but are also important in relation to the finite measurement durations. Evaluation of the expression obtained in section 4 reveals an additional dependence on the correction factors that are needed to adjust the Bernouilli model for temporal integration (Fig. 2).

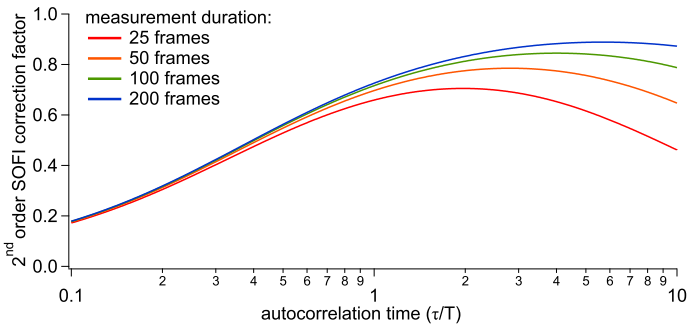

Fig. 2. The effect of limited measurement duration on the correction factor on the Bernoulli model, taking both fast switching and a limited measurement duration into account.

6. Validation of the proposed model

The strength of our model is that it can quantitatively predict the SOFI images that result under conditions that closely approximate the real world. However, its absolute accuracy is difficult to verify on actual experimental data since the underlying ground truth fluorophore distribution and properties are unknown in actual samples. We therefore turned to numerical simulations of the imaging process, since the photophysics of blinking and the fluorescence imaging process are known well enough to enable highly accurate simulation. Our simulation methodology was previously explained in e.g. Ref. [20].

Figure 3 shows the results of a numerical simulation, in which single emitters were randomly distributed over a surface. The sample was further divided into three distinct regions, showing different emitter blinking kinetics. Panels (A) and (D) show the results of explicitly simulating

Optics EXPRESS

the imaging process over 10,000 fluorescence images, and then calculating SOFI images from these images using the standard calculation methodology and for two different lag times. These images are taken to be the ground truth SOFI images.

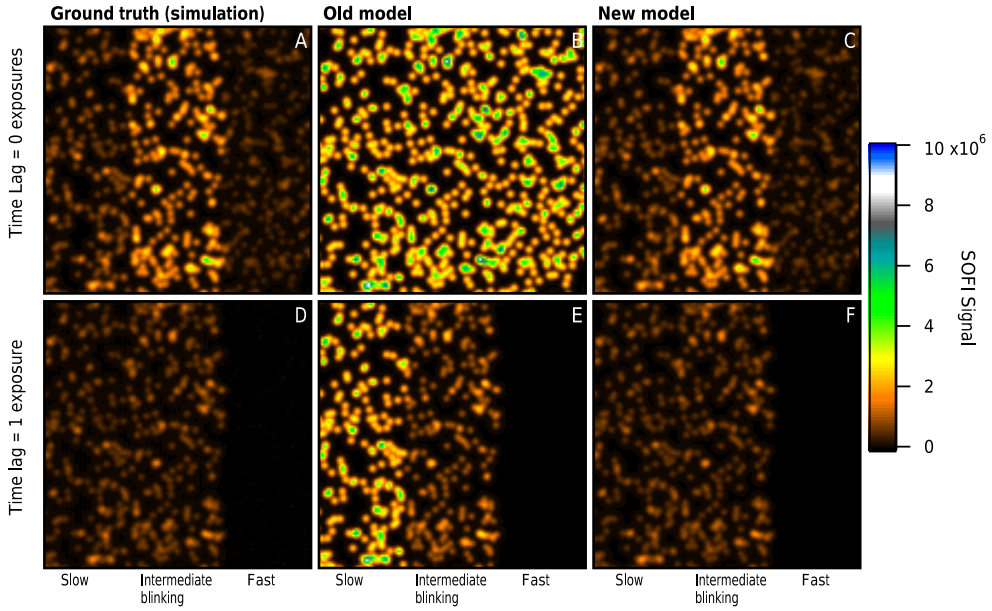

Fig. 3. The effect of limited measurement duration on the correction factor on the Bernoulli model, taking both fast switching and a limited measurement duration into account.

Panels (B) and (E) show the expected SOFI images calculated using the previous SOFI model, while panels (C) and (F) show the expected SOFI images predicted by the new model introduced here. These results clearly show that the images predicted by the previous model strongly diverge from the ground truth due to the unrealistic nature of its assumptions. Our improved model, in contrast, essentially perfectly reproduces the ground truth. Furthermore, the improved model executes about two orders of magnitude faster than the simulations, despite our simulation code having been heavily optimized over the years. This very fast performance opens the door to more advanced analysis strategies, as could be based on e.g. iterative optimization of calculated SOFI images to match experimental results.

We next sought to compare our model with actual measurement data, though this is complicated by the fact that the associated ground truth emitter distribution is unknown in actual samples. We reasoned instead that we could evaluate the temporal dependence of the SOFI signal, since this is mainly determined by the nature of the labels and not their spatial distribution, yet does depend on the full intricacies of the SOFI calculation. We previously showed how the kinetics of the fluorophore dynamics can be used to resolve different types of emitters in SOFI, using an approach that we termed multiple-tau SOFI (mtSOFI) [23]. The key insight from this work was that the SOFI signal generally decreases for increasing lag times, but that the rate of this decrease depends on the switching kinetics of the fluorophores. Since the contribution of each emitter can be distinguished based on the decay for the increasing lag times, emitters with different kinetics can be separated even if their emission spectra overlap [23].

The previous model for SOFI images predicts that this decay can be described using an exponential function, but our measurements showed strong deviations from this simple model (Fig. 4). This was problematic because the correct emitter separation depends crucially on the definition of appropriate filter functions [23]. In this publication, we resolved this by conducting

Optics EXPRESS

extensive and time-consuming numerical simulations to determine the probe parameters and optimize the imaging process. However, our improved model readily allows the reproduction of the measured data, and associated determination of the fluorophore blinking parameters. Overall this allows us to obtain more reliable results in a much shorter time.

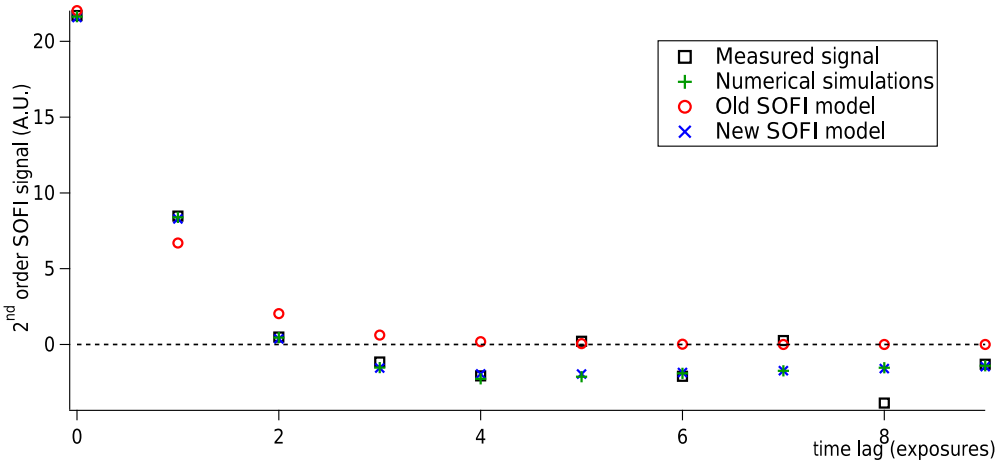

Fig. 4. Measured SOFI signal on a live HeLa cell expressing rsGreen1, and as a function of time lag (full details can be found in Appendix D). The signal from a single detector pixel is shown. Also shown are the best fits of this data using the previous SOFI, the model presented here, and numerical simulations.

7. Conclusions

In this contribution we have sought to develop a quantitative model for SOFI imaging that is compatible with the limitations inherent in actual experiments. Our model can efficiently predict the SOFI image resulting from arbitrary instrumental parameters, sample structuring, and probe dynamics. Our model supersedes prior methods by allowing us to include the spatially- and temporarily-integrating nature of real-world detectors, the finite duration of actual imaging experiments, and arbitrary models for the fluorescence dynamics. It also delivers vast performance improvements compared to numerical simulations of the imaging process.

Our model delivers a number of key insights. For second and third order SOFI imaging, we find that SOFI images are reliable in the sense that they are absolutely proportional to concentration if all emitters display the same dynamics (this assumption is also required for proportionality in classical imaging). Brightness differences between different parts of the image or between different images can be directly interpreted as changes in concentration. However, including a finite number of fluorescence images does introduce a systematic bias into the cumulant calculation, which means that the proportionality constant also depends on the number of raw fluorescence images included in the SOFI calculation. Strictly speaking, this means that only SOFI images calculated from the same number of fluorescence images can be quantitatively compared, though in practical terms this is most likely the case by default because all practical implementations of the SOFI algorithm rely on 'batching' of the calculation to reduce the influence of photodestruction. This means that SOFI images are calculated over small groups of fluorescence images, and then averaged together.

For fourth- and higher-order calculations, this proportionality is no longer strictly assured as the cumulant calculation is then no longer an unbiased estimator of the true cumulant. Any discrepancy will get smaller as the number of fluorescence images in the calculation increases,

Optics EXPRESS

which requires that the batch sizes are not made smaller than strictly necessary. In principle, the cumulant calculation could be reworked to obtain an unbiased estimator, though this is outside the scope of this contribution.

Our model can be readily applied in practice. Due to the additivity of cumulants, this amounts to calculating the contribution of a single fluorophore to the SOFI image, and then summing the contributions of all fluorophores in a per-pixel manner. Applying our model in practice reduces to knowing the point-spread function of the microscope on the one hand, and the cumulants of the on-time ratio distribution of the fluorophores (shared between all fluorophores with the same dynamics) on the other. Efficient analytical expressions exist for Gaussian PSFs and exponential switching between fluorescent and non-fluorescent states. Non-Gaussian PSFs can be readily added using numerical integration, as is customarily required, while other probe dynamics can be added by either calculating the cumulants directly, or obtaining these using numerical simulations.

By correctly and efficiently taking the probe and measurement properties into account, our model opens the door to more advanced SOFI analysis methodologies, in which probe parameters and distributions are iteratively reconstructed from SOFI images of different orders. Similarly, our model provides the quantitative formalism for the use of SOFI as a tool to unravel nanoscale biological contexts based on changes in probe dynamics.

Appendix A: Cumulants with repeat pixels

These equations are a continuation of Eqs. 19–26 in the main text, relating to the effect of repeat pixels on the cumulants.

Low read-out noise sensors

$$C_3(X_1, X_1, X_{1,\delta_1}) = \lambda_1^3 C_3(\rho, \rho, \rho_{\delta_1}) + C_2(X_1, X_{1,\delta_1}) \tag{38}$$

$$C_3(X_1, X_1, X_2) = \lambda_1^2 \lambda_2 C_3(\rho) + C_2(X_1, X_2) \tag{39}$$

$$\begin{aligned} C_4(X_1, X_1, X_1, X_{1,\delta_1}) = \lambda_1^4 C_4(\rho, \rho, \rho, \rho_{\delta_1}) \\ + 3C_3(X_1, X_1, X_{\delta_1}) - 2C_2(X_1, X_{1,\delta_1}) \end{aligned} \tag{40}$$

$$C_4(X_1, X_1, X_1, X_2) = \lambda_1^3 \lambda_2 C_4(\rho) + 3C_3(X_1, X_1, X_2) - 2C_2(X_1, X_2) \tag{41}$$

$$\begin{aligned} C_4(X_1, X_1, X_2, X_2) = \lambda_1^2 \lambda_2^2 C_4(\rho) \\ + C_3(X_1, X_1, X_2) + C_3(X_1, X_2, X_2) - C_2(X_1, X_2) \end{aligned} \tag{42}$$

$$C_4(X_1, X_1, X_2, X_3) = \lambda_1^2 \lambda_2 \lambda_3 C_4(\rho) + C_3(X_1, X_2, X_3) \tag{43}$$

$$C_4(X_1, X_1, X_{1,\delta_1}, X_{1,\delta_2}) = \lambda_1^4 C_4(\rho, \rho, \rho_{\delta_1}, \rho_{\delta_2}) + C_3(X_1, X_{1,\delta_1}, X_{1,\delta_2}) \tag{44}$$

Electron-multiplying sensors

$$C_3(X_1, X_1, X_{1,\delta_1}) = \gamma^3 \lambda_1^3 C_3(\rho, \rho, \rho_{\delta_1}) + 2\gamma C_2(X_1, X_{1,\delta_1}) \tag{45}$$

$$C_3(X_1, X_1, X_2) = \gamma^3 \lambda_1^2 \lambda_2 C_3(\rho) + 2\gamma C_2(X_1, X_2) \tag{46}$$

$$\begin{aligned} C_4(X_1, X_1, X_1, X_{1,\delta_1}) = \gamma^4 \lambda_1^4 C_4(\rho, \rho, \rho, \rho_{\delta_1}) \\ + 6\gamma C_3(X_1, X_1, X_{\delta_1}) - 6\gamma^2 C_3(X_1, X_{1,\delta_1}) \end{aligned} \tag{47}$$

$$\begin{aligned} C_4(X_1, X_1, X_1, X_2) = \gamma^4 \lambda_1^3 \lambda_2 C_4(\rho) \\ + 6\gamma C_3(X_1, X_1, X_2) - 6\gamma^2 C_3(X_1, X_2) \end{aligned} \tag{48}$$

$$\begin{aligned} C_4(X_1, X_1, X_2, X_2) = \gamma^4 \lambda_1^2 \lambda_2^2 C_4(\rho) + 2\gamma C_3(X_1, X_1, X_2) \\ + 2\gamma C_3(X_1, X_2, X_2) - 4\gamma^2 C_2(X_1, X_2) \end{aligned} \tag{49}$$

$$C_4(X_1, X_1, X_2, X_3) = \gamma^4 \lambda_1^2 \lambda_2 \lambda_3 C_4(\rho) + 2\gamma C_3(X_1, X_2, X_3) \tag{50}$$

$$C_4(X_1, X_1, X_{1,\delta_1}, X_{1,\delta_2}) = \gamma^4 \lambda_1^4 C_4(\rho, \rho, \rho_{\delta_1}, \rho_{\delta_2}) + 2\gamma C_3(X_1, X_{1,\delta_1}, X_{1,\delta_2}) \tag{51}$$

Optics EXPRESS

Appendix B: Effect of measurement duration in third-order SOFI

The calculation that follows mirrors that for second order in section 3.4.

$$\begin{aligned} C_3(X_1,X_2,X_3) &= \mathbb{E}\{X_1X_2X_3\} + 2\,\mathbb{E}\{X_1\}\,\mathbb{E}\{X_2\}\,\mathbb{E}\{X_3\} \\ &\quad - \mathbb{E}\{X_1X_2\}\,\mathbb{E}\{X_3\} - \mathbb{E}\{X_1X_3\}\,\mathbb{E}\{X_2\} - \mathbb{E}\{X_2X_3\}\,\mathbb{E}\{X_1\} \end{aligned} \tag{52}$$

$$\begin{aligned} c_3(X_1,X_2,X_3) &= \frac{1}{N}\sum_{n=1}^{N}(X_{1,n}X_{2,n}X_{3,n}) + \frac{2}{N^3}\sum_{n=1}^{N}X_{1,n}\sum_{n=1}^{N}X_{2,n}\sum_{n=1}^{N}X_{3,n} \\ &\quad - \frac{1}{N^2}\sum_{n=1}^{N}(X_{1,n}X_{2,n})\sum_{n=1}^{N}X_{3,n} - \frac{1}{N^2}\sum_{n=1}^{N}(X_{1,n}X_{3,n})\sum_{n=1}^{N}X_{2,n} \\ &\quad - \frac{1}{N^2}\sum_{n=1}^{N}(X_{2,n}X_{3,n})\sum_{n=1}^{N}X_{1,n} \end{aligned} \tag{53}$$

$$\begin{aligned} \mathbb{E}\{c_3(X_1,X_2,X_3)\} &= \frac{1}{N}\mathbb{E}\{X_{1,t}X_{2,t}X_{3,t}\} + \frac{2}{N^3}\sum_{i=1}^{N}\sum_{j=1}^{N}\sum_{k=1}^{N}\mathbb{E}\{X_1X_{2,(j-i)}X_{3,(k-i)}\} \\ &\quad - \frac{1}{N^2}\sum_{i=1}^{N}\sum_{j=1}^{N}\Big(\mathbb{E}\{X_1X_2X_{3,(j-i)}\} + \mathbb{E}\{X_1X_{2,(j-i)}X_3\} + \mathbb{E}\{X_{1,(j-i)}X_2X_3\}\Big) \end{aligned} \tag{54}$$

This equation is expanded and the following substitutions are made

$$\begin{aligned} \mathbb{E}\{X_{1,i}X_{2,j}X_{3,k}\} &= C_3(X_{1,i},X_{2,j},X_{3,k}) - 2\,\mathbb{E}\{X_1\}\,\mathbb{E}\{X_2\}\,\mathbb{E}\{X_3\} \\ &\quad - \mathbb{E}\{X_{1,i}X_{2,j}\}\,\mathbb{E}\{X_3\} - \mathbb{E}\{X_{1,i}X_{3,k}\}\,\mathbb{E}\{X_2\} - \mathbb{E}\{X_{2,j}X_{3,k}\}\,\mathbb{E}\{X_1\} \end{aligned} \tag{55}$$

Noting that the lower order terms cancel out we then obtain.

$$\begin{aligned} \mathbb{E}\{c_3(X_1,X_2,X_3)\} &= \left(\frac{n}{n} + \frac{2n}{n^3} - \frac{3n}{n^2}\right)C_3(X_1,X_2,X_3) \\ &+ \sum_{j=1}^{j=n-1}\left(\frac{2\,(n-j)}{n^3} - \frac{n-j}{n^2}\right)\Big(C_3(X_1,X_{2,\delta_j},X_3) + C_3(X_1,X_{2,\delta_{-j}},X_3)\Big) \\ &+ \sum_{j=1}^{j=n-1}\left(\frac{2\,(n-j)}{n^3} - \frac{n-j}{n^2}\right)\Big(C_3(X_1,X_2,X_{3,\delta_j}) + C_3(X_1,X_2,X_{3,\delta_{-j}})\Big) \\ &+ \sum_{j=1}^{j=n-1}\left(\frac{2\,(n-j)}{n^3} - \frac{n-j}{n^2}\right)\Big(C_3(X_1,X_{2,\delta_j},X_{3,\delta_j}) + C_3(X_1,X_{2,\delta_{-j}},X_{3,\delta_{-j}})\Big) \\ &+ \sum_{i=1}^{i=n-1}\sum_{j=i+1}^{j=n-1}\frac{2\,(n-j)}{n^3}\Big(C_3(X_1,X_{2,\delta_i},X_{3,\delta_j}) + C_3(X_1,X_{2,\delta_j},X_{3,\delta_i})\Big) \\ &+ \sum_{i=1}^{i=n-1}\sum_{j=i+1}^{j=n-1}\frac{2\,(n-j)}{n^3}\Big(C_3(X_1,X_{2,\delta_{-i}},X_{3,\delta_{j-i}}) + C_3(X_1,X_{2,\delta_{-j}},X_{3,\delta_{i-j}})\Big) \\ &+ \sum_{i=1}^{i=n-1}\sum_{j=i+1}^{j=n-1}\frac{2\,(n-j)}{n^3}\Big(C_3(X_1,X_{2,\delta_{j-i}},X_{3,\delta_{-i}}) + C_3(X_1,X_{2,\delta_{i-j}},X_{3,\delta_{-j}})\Big) \end{aligned} \tag{56}$$

Showing that, as for second order, we obtain a valid SOFI image, though one that is a linear combination of the SOFI images for all time lags.

Optics EXPRESS

Appendix C: Derivation of Cumulants for the Temporally integrated two-state model

We are interested in the cumulants of the on-time ratio distribution for a molecule alternating between two states (on and off) with transition rates $k_{\text{on}\to\text{off}}$ and $k_{\text{off}\to\text{on}}$ being constant over the entire experiment, where the transitions are in no way synchronized to the camera exposures. This situation matches with models existing for the fraction of time a computer system is up in any given period, i.e. the duration of the maintenance contract as shown in Kirmani et al. [30], where the interval availability i corresponds to the on-time ratio during a single exposure interval.

In [30] equations for $\mathbb{E}\{i\} \equiv \mathbb{E}\{\rho\}$ and $\mathbb{E}\left\{i^2\right\} \equiv \mathbb{E}\left\{\rho^2\right\}$ are given in a way that is trivial to extend to any $\mathbb{E}\{\rho^n\}$ for a system which is in the on state at the start of a frame exposure. We will refer to these expectation values as $\mathbb{E}_{\text{on}}\{\rho^n\}$. Since at this point there is no special difference between the on and off state the following symmetry argument can be made:

$$\mathbb{E}_{\text{off}}\{(1-\rho)^n\} \equiv \mathbb{E}_{\text{on}}\{\rho^n\} \text{ with swapped } k_{\text{on}\to\text{off}} \text{ and } k_{\text{off}\to\text{on}}.$$

$\mathbb{E}_{\text{off}}\{\rho^n\}$ can then be obtained from $\mathbb{E}_{\text{off}}\{(1-\rho)^n\}$ by the linearity of the expectation operator.

$$\mathbb{E}_{\text{off}}\{1-\rho\} = 1 - \mathbb{E}_{\text{off}}\{\rho\} \Rightarrow \mathbb{E}_{\text{off}}\{\rho\} = 1 - \mathbb{E}_{\text{off}}\{1-\rho\} \tag{57}$$

$$\begin{aligned}\mathbb{E}_{\text{off}}\left\{(1-\rho)^2\right\} = 1 - 2\,\mathbb{E}_{\text{off}}\{\rho\} + \mathbb{E}_{\text{off}}\left\{\rho^2\right\} \Rightarrow \mathbb{E}_{\text{off}}\left\{\rho^2\right\} &= 1 - 2\,\mathbb{E}_{\text{off}}\{1-\rho\} \\ &+ \mathbb{E}_{\text{off}}\left\{(1-\rho)^2\right\}\end{aligned} \tag{58}$$

The unconditional moments $\mathbb{E}\{\rho^n\}$ are now obtained by applying the linearity of the expectation operator again.

$$\mathbb{E}\{\rho^n\} = \widehat{\rho}\,\mathbb{E}_{\text{on}}\{\rho^n\} + (1-\widehat{\rho})\,\mathbb{E}_{\text{off}}\{\rho^n\} \tag{59}$$

These moments can be converted to cumulants using the methodology and formulas given in [24].

To obtain time-lagged moments that can be converted to time-lagged cumulants, we make use of the observation that there is no difference between a moment conditional on the state at the beginning of a frame and a moment conditional on the state at the end of the frame. That is $\mathbb{E}_{\text{on}}\{\rho^n\}$ is valid for both a molecule starting or ending in the on state. Therefore, we can immediately define the moments for a single-frame time lag by conditioning the state of the molecule at the end of the first frame:

$$\mathbb{E}\left\{\rho^m\rho_\delta^n\right\} = \mathbb{E}_{\text{on}}\{\rho^m\}\,\widehat{\rho}\,\mathbb{E}_{\text{on}}\{\rho^n\} + \mathbb{E}_{\text{off}}\{\rho^m\}\,(1-\widehat{\rho})\,\mathbb{E}_{\text{off}}\{\rho^n\} \tag{60}$$

$$\begin{aligned}\mathbb{E}\left\{\rho^m\rho_\delta^n\right\} = &\ \widehat{\rho}\,\mathbb{E}_{\text{on}}\{\rho^m\}\,P_{\text{on}\to\text{on}}(\delta)\,\mathbb{E}_{\text{on}}\{\rho^n\} \\ &+ \widehat{\rho}\,\mathbb{E}_{\text{on}}\{\rho^m\}\,P_{\text{on}\to\text{off}}(\delta)\,\mathbb{E}_{\text{off}}\{\rho^n\} \\ &+ (1-\widehat{\rho})\,\mathbb{E}_{\text{off}}\{\rho^m\}\,P_{\text{off}\to\text{on}}(\delta)\,\mathbb{E}_{\text{on}}\{\rho^n\} \\ &+ (1-\widehat{\rho})\,\mathbb{E}_{\text{off}}\{\rho^m\}\,P_{\text{off}\to\text{off}}(\delta)\,\mathbb{E}_{\text{off}}\{\rho^n\}\end{aligned} \tag{61}$$

Unfortunately the mechanism by which we derive these cumulants does not allow for us to obtain formulas with more than one time lag. This not only limits the direct results, but also means that for the most complete form of the SOFI formulas incorporating the limited measurement time we can only give a complete formula for the second-order cumulant.

Appendix D: testing the validity of the model

For testing the validity of the model (shown in Fig. 4) a comparison was made between the fit of experimental data using the model derived in this paper, or an exponential model which was previously seen as the state of the art. The overall trend is well replicated using the novel

Optics EXPRESS

model, however at longer lag time some variation is observed. To prove that our model is consistent with two state switching, simulations were added which match the analytical data perfectly. The experimental data was obtained as described in [23]. Briefly, HeLa cells were cultured at 37°C in the presence of 5%CO_2 in DMEM supplemented with 10% (v/v) FBS, 2mM glutaMAX^{TM} and 0.1% (v/v) gentamicin (all Gibco). Before transfection, approximately 250000 cells were seeded in a 35mm glass bottom dish (MatTek) and grown to 80% confluency. Cells were transfected using FuGene6 (Promega) according to manufacturers instructions with 1μg of prsGreen1-MAP4 plasmid DNA. The plasmid was constructed by replacing the mCherry gene with the gene encoding rsGreen1 in the mCherry-MAP4-N-10 plasmid, which was a gift from Michael Davidson (Addgene plasmid # 55076). Cells were imaged approximately 24 hours post transfection in Hanks' balanced salt solution after washing three times with phosphate buffered saline. Imaging was performed on an Olympus IX83 inverted microscope equipped with a 150× UAPON OTIRF objective, an ImagEM X2 EMCCD camera (Hamamatsu), a Di01-R405/488/561/635 polychroic mirror, a FF01-446/523/600/677 emission filter (both Semrock) and a cell^{TIRF} TIRF module coupling in a 150mW 488nm cell* laser. Datasets of 1000 frames were acquired in epi configuration with 488nm excitation (approximately 3mW measured at the back aperture of the objective), using an exposure time of 8 ms and an EM gain of 500.

The simulation was preformed as described in [7,15,19,20]. Briefly, 10000 molecules where randomly positioned in a grid of 64 by 64 pixels, and random 2 state switching was simulated for 10000 frames at an exposure time of 10 ms and a molecular brightness of 20000 photons per second. The average on- and off-times where set to obtain $\tau = 0.73$ frames and an on-time-ratio $\rho = 10\,\%$. At this point the correlation curves for the simulation as well as the experimental data where constructed by performing second order SOFI calculations at different lag times with a batch (or substack) size of 50 frames. The average signal over the image stack was plotted in respect to the lag time, with the simulation curve scaled to match the experimental decay at lag 0.

For the data shown in Fig. 3 10000 molecules where spread over a 64×64 pixel grid, with each emitting 100000 detected photons per second in the on-state. The leftmost molecules where set to have an average lifetimes of 100 ms and 1000 ms in the on- and off-state respectively with both lifetimes being reduced by a factor of 10 for each subsequent band, they where assumed to emit at 520nm to be collected by an objective with an NA of 1.4 and imaged with a projected pixel size of 100nm. At this point 10000 images where simulated at an exposure time of 10 ms which where calculated to yield a lag = 0 frames and lag = 1 frame SOFI image. For both models these same parameters where used to calculate the SOFI images. For the old model this means an exponential dependence on time-lag with τ as a characteristic decay time where combined with the uncorrected Bernoulli model and a Gaussian (unintegrated) PSF. For the new model the corrections of Eqs. (31)–(32) and the correction of Fig. 1 where included, and the Gaussian was set to integrate over the pixel area as in Eq. (33).

Funding

Fonds Wetenschappelijk Onderzoek (G0B8817N); ERC (714688).

Acknowledgments

S.D. acknowledges a post-doctoral fellowship from the Research Foundation Flanders (FWO). We are grateful to Prof. Theo Lasser and Dr. Stefan Geissbühler (Laboratoire d'Optique Biomédicale, École Polytechnique Fédérale de Lausanne, Switzerland) for early discussions and exchanges of ideas. M.L. thanks Prof. Stefan W. Hell for the research position in his department. W.V. thanks Prof. Cyril Ruckebusch for discussion.

Optics EXPRESS

References

1. T. Dertinger, R. Colyer, G. Iyer, S. Weiss, and J. Enderlein, "Fast, background-free, 3D super-resolution optical fluctuation imaging (SOFI)," Proc. Natl. Acad. Sci. **106**(52), 22287–22292 (2009).
2. S. Geissbuehler, C. Dellagiacoma, and T. Lasser, "Comparison between SOFI and STORM," Biomed. Opt. Express **2**(3), 408–420 (2011).
3. H. Deschout, T. Lukeš, A. Sharipov, D. Szlag, L. Feletti, W. Vandenberg, P. Dedecker, J. Hofkens, M. Leutenegger, T. Lasser, and A. Radenovic, "Complementarity of PALM and SOFI for super-resolution live-cell imaging of focal adhesions," Nat. Commun. **7**(1), 13693–00 (2016).
4. A. Girsault, T. Lukeš, A. Sharipov, S. Geissbuehler, M. Leutenegger, W. Vandenberg, P. Dedecker, J. Hofkens, and T. Lasser, "SOFI simulation tool: a software package for simulating and testing super-resolution optical fluctuation imaging," PLoS One **11**(9), e0161602–0 (2016).
5. W. Vandenberg, M. Leutenegger, T. Lasser, J. Hofkens, and P. Dedecker, "Diffraction-unlimited imaging: from pretty pictures to hard numbers," Cell Tissue Res. **360**(1), 151–178 (2015).
6. P. Dedecker, S. Duwé, R. K. Neely, and J. Zhang, "Localizer: fast, accurate, open-source, and modular software package for superresolution microscopy," J. Biomed. Opt. **17**(12), 126008 (2012).
7. W. Vandenberg, S. Duwé, M. Leutenegger, B. Moeyaert, B. Krajnik, T. Lasser, and P. Dedecker, "Model-free uncertainty estimation in stochastical optical fluctuation imaging (SOFI) leads to a doubled temporal resolution," Biomed. Opt. Express **7**(2), 467–480 (2016).
8. B. Moeyaert, N. Nguyen Bich, E. De Zitter, S. Rocha, K. Clays, H. Mizuno, L. van Meervelt, J. Hofkens, and P. Dedecker, "Green-to-red photoconvertible dronpa mutant for multimodal super-resolution fluorescence microscopy," ACS Nano **8**(2), 1664–1673 (2014).
9. F. Hertel, G. C. Mo, S. Duwé, P. Dedecker, and J. Zhang, "RefSOFI for mapping nanoscale organization of protein-protein interactions in living cells," Cell Rep. **14**(2), 390–400 (2016).
10. G. C. Mo, B. Ross, F. Hertel, P. Manna, X. Yang, E. Greenwald, C. Booth, A. M. Plummer, B. Tenner, Z. Chen, Y. Wang, E. J. Kennedy, P. A. Cole, K. G. Fleming, A. Palmer, R. Jimenez, J. Xiao, P. Dedecker, and J. Zhang, "Genetically encoded biosensors for visualizing live-cell biochemical activity at super-resolution," Nat. Methods **14**(4), 427–434 (2017).
11. T. Lukeš, J. Pospíšil, K. Fliegel, T. Lasser, and G. Hagen, "Quantitative super-resolution single molecule microscopy dataset of YFP-tagged growth factor receptors," GigaScience **7**(3), giy002 (2018).
12. S. Geissbuehler, A. Sharipov, A. Godinat, N. L. Bocchio, P. A. Sandoz, A. Huss, N. A. Jensen, S. Jakobs, J. Enderlein, F. Gisou van der Goot, E. A. Dubikovskaya, T. Lasser, and M. Leutenegger, "Live-cell multiplane three-dimensional super-resolution optical fluctuation imaging," Nat. Commun. **5**(1), 5830 (2014).
13. A. Descloux, K. Grußmayer, E. Bostan, T. Lukeš, A. Bouwens, A. Sharipov, S. Geissbuehler, A. Mahul-Mellier, H. Lashuel, M. Leutenegger, and T. Lasser, "Combined multi-plane phase retrieval and super-resolution optical fluctuation imaging for 4D cell microscopy," Nat. Photonics **12**(3), 165–172 (2018).
14. A. Purohit, W. Vandenberg, T. Dertinger, P. Dedecker, and J. Enderlein, "Spatio-temporal correlation super-resolution optical fluctuation imaging," EPL **125**(2), 20005 (2019).
15. P. Dedecker, G. C. Mo, T. Dertinger, and J. Zhang, "Widely accessible method for superresolution fluorescence imaging of living systems," Proc. Natl. Acad. Sci. U. S. A. **109**(27), 10909–10914 (2012).
16. J. Widengren, "Fluorescence-based transient state monitoring for biomolecular spectroscopy and imaging," J. R. Soc., Interface **7**(49), 1135–1144 (2010).
17. T. Dertinger, R. Colyer, R. Vogel, J. Enderlein, and S. Weiss, "Achieving increased resolution and more pixels with superresolution optical fluctuation imaging (SOFI)," Opt. Express **18**(18), 18875–18885 (2010).
18. S. Geissbuehler, N. L. Bocchio, C. Dellagiacoma, C. Berclaz, M. Leutenegger, and T. Lasser, "Mapping molecular statistics with balanced super-resolution optical fluctuation imaging (bSOFI))," Biomed. Opt. Phase Microsc. Nanosc. **1**(1), 4 (2012).
19. W. Vandenberg and P. Dedecker, "Effect of probe diffusion on the SOFi imaging accuracy," Sci. Rep. **7**(1), 44665 (2017).
20. Y. Peeters, W. Vandenberg, S. Duwé, A. Bouwens, T. Lukeš, C. Ruckebusch, T. Lasser, and P. Dedecker, "Correcting for photodestruction in super-resolution optical fluctuation imaging," Sci. Rep. **7**(1), 10470 (2017).
21. T. Lukeš, D. Glatzova, Z. Kvicalova, F. Levet, A. Benda, T. Brdicka, T. Lasser, and M. Cebecauer, "Quantifying protein densities on cell membranes using super-resolution optical fluctuation imaging," Nat. Commun. **8**(1), 1731 (2017).
22. S. C. Stein, A. Huss, D. Hahnel, I. Gregor, and J. Enderlein, "Fourier interpolation stochastic optical fluctuation imaging," Opt. Express **23**(12), 16154–16163 (2015).
23. S. Duwé, W. Vandenberg, and P. Dedecker, "Live-cell monochromatic dual-label sub-diffraction microscopy by mt-pcSOFI," Chem. Commun. **53**(53), 7242–7245 (2017).
24. A. Stuart and K. Ord, *Kendall's advanced theory of statistics*, vol. I (Wiley, 2009).
25. M. Hirsch, R. J. Wareham, M. L. Martin-Fernandez, M. P. Hobson, and D. J. Rolfe, "A stochastic model for electron multiplication charge-coupled devices–from theory to practice," PLoS One **8**(1), e53671 (2013).
26. S. Duwé, E. De Zitter, V. Gielen, B. Moeyaert, W. Vandenberg, T. Grotjohann, K. Clays, S. Jakobs, L. Van Meervelt, and P. Dedecker, "Expression-enhanced fluorescent proteins based on enhanced green fluorescent protein for super-resolution microscopy," ACS Nano **9**(10), 9528–9541 (2015).

Optics EXPRESS

27. T. Dertinger, M. Heilemann, R. Vogel, M. Sauer, and S. Weiss, "Superresolution optical fluctuation imaging with organic dyes," Angew. Chem., Int. Ed. **49**(49), 9441–9443 (2010).
28. X. Zhang, X. Chen, Z. Zeng, M. Zhang, Y. Sun, P. Xi, J. Peng, and P. Xu, "Development of a reversibly switchable fluorescent protein for super-resolution optical fluctuation imaging (SOFI)," ACS Nano **9**(3), 2659–2667 (2015).
29. A. M. Chizhik, S. Stein, M. O. Dekaliuk, C. Battle, W. Li, A. Huss, M. Platen, I. A. Schaap, I. Gregor, A. P. Demchenko, C. F. Schmidt, J. Enderlein, and A. I. Chizhik, "Super-resolution optical fluctuation bio-imaging with dual-color carbon nanodots," Nano Lett. **16**(1), 237–242 (2016).
30. E. Kirmani and C. S. Hood, "A new approach to analysis of interval availability," in *ARES 2008 - 3rd International Conference on Availability, Security, and Reliability, Proceedings*, (IEEE Computer Society, 2008), pp. 479–483.